

Ionization Energy of the Metastable 2^1S_0 State of ^4He from Rydberg-Series Extrapolation

Gloria Clausen[✉], Paul Jansen, Simon Scheidegger, Josef A. Agner, Hansjürg Schmutz, and Frédéric Merkt^{✉*}
Laboratory of Physical Chemistry, ETH Zurich, CH-8093 Zurich, Switzerland

 (Received 28 April 2021; accepted 12 July 2021; published 27 August 2021)

In a recent breakthrough in first-principles calculations of two-electron systems, Patkóš, Yerokhin, and Pachucki [Phys. Rev. A **103**, 042809 (2021)] have performed the first complete calculation of the Lamb shift of the helium 2^3S_1 and 2^3P_J triplet states up to the term in α^7m . Whereas their theoretical result of the frequency of the $2^3P \leftarrow 2^3S$ transition perfectly agrees with the experimental value, a more than 10σ discrepancy was identified for the $3^3D \leftarrow 2^3S$ and $3^3D \leftarrow 2^3P$ transitions, which hinders the determination of the He^{2+} charge radius from atomic spectroscopy. We present here a new measurement of the ionization energy of the 2^1S_0 state of He [960 332 040.491(32) MHz] which we use in combination with the $2^3S_1 \leftarrow 2^1S_0$ interval measured by Rengelink *et al.* [Nat. Phys. **14**, 1132 (2018).] and the $2^3P \leftarrow 2^3S_1$ interval measured by Zheng *et al.* [Phys. Rev. Lett. **119**, 263002 (2017)] and Cancio Pastor *et al.* [Phys. Rev. Lett. **92**, 023001 (2004)] to derive experimental ionization energies of the 2^3S_1 state [1152 842 742.640(32) MHz] and the 2^3P centroid energy [876 106 247.025(39) MHz]. These values reveal disagreements with the α^7m Lamb shift prediction by 6.5σ and 10σ , respectively, and support the suggestion by Patkóš *et al.* of an unknown theoretical contribution to the Lamb shifts of the 2^3S and 2^3P states of He.

DOI: 10.1103/PhysRevLett.127.093001

In recent years, intensive efforts have been invested in ultraprecise calculations and measurements of energy intervals in the light atoms and molecules H [1–6], H_2^+ and HD^+ [7–9], He [10–17], H_2 [18,19], and He_2^+ [20–22]. These efforts aim at testing and validating first-principles relativistic and quantum-electrodynamics calculations in light systems containing only few electrons [23,24]. For these few-body systems, the theoretical and computational frameworks are so advanced that predictions of energy intervals can be made at precisions corresponding to (much) more than ten significant digits. The task of experimentalists is to develop procedures and carry out measurements that achieve the same precision.

If experimental and theoretical results agree, their combination offers the prospect of improving the values of fundamental constants and particle properties. Discrepancies may reveal incomplete aspects of the theoretical treatment or point at unrecognized interactions and challenge the standard model of particle physics.

Remarkable recent achievements in one-electron systems include (i) a significant update of the values of the Rydberg constant and the proton charge radius from precision measurements in H and muonic hydrogen [1–6,23,25], and (ii) the determination of the proton-to-electron mass ratio from precision measurements of vibrational-energy intervals in HD^+ [7–9].

The two-electron systems He and H_2 (and HD and D_2) are becoming increasingly attractive, despite the theoretical complications arising from electron-correlation effects. Agreement in the theoretical and experimental values of

the dissociation energy of H_2 has reached the precision level of 10^{-11} [18,19], making this molecule a “cornerstone of ultraprecise quantum chemistry” [19].

Recently, Patkóš *et al.* [12] have reported the first complete calculation of the α^7m Lamb shift in He triplet states, which reached agreement with experimental results on the $2^3P \leftarrow 2^3S$ [15] interval within the uncertainty of the theoretical result (54 kHz or 2×10^{-10} relative accuracy) [12]. At the same time, Patkóš *et al.* pointed at discrepancies between experiment and theory concerning the $3^3D_1 \leftarrow 2^3S_1$ [26] and $3^3D_1 \leftarrow 2^3P_0$ [14] intervals, in excess of 10σ for the latter interval. This discrepancy hinders the determination of the α -particle charge radius from He spectroscopy to complement the recent determination in muonic helium [27] and requires urgent attention. Zalialutdinov *et al.* [28] have suggested that the discrepancy might be explained by quantum-interference shifts affecting the experimental transition frequencies to the 3^3D_1 level.

We report on a new determination of the ionization energy of the 2^1S_0 metastable state of He at a precision of 32 kHz (or 3×10^{-11}) by extrapolation of the singlet np Rydberg series. The significance of this new measurement is that it enables (i) the direct comparison with earlier experimental [29–31] and theoretical results [10,11] of this quantity and, more importantly, (ii) the determination of purely experimental values for the ionization energies of the 2^3S_1 and 2^3P states of He by combination with earlier ultraprecise measurements of the $2^3S_1 \leftarrow 2^1S_0$ [17] and the $2^3P \leftarrow 2^3S_1$ [15,32,33] transitions (see Fig. 1) to test the

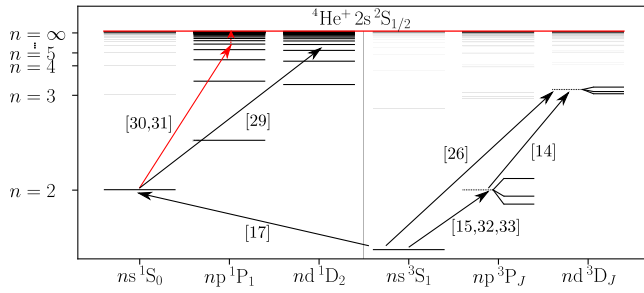


FIG. 1. Level diagram of the He singlet states (left) and triplet states (right) with the relevant transitions from literature marked as full arrows [14,15,17,26,29–33]. The horizontal dashed lines mark the centroid positions of the $2p^3P_J$ and $3d^3D_J$ levels. A vertical measurement is indicated by the red arrow and the dashed vertical arrow shows the extrapolation to the ${}^4\text{He}^+ 1s^2S_{1/2}$ state (red horizontal line).

calculations of Patkóš *et al.* [12]. Finally, (iii) transitions to singlet states are not affected by quantum-interference effects [2,28] between fine-structure components.

The experimental setup is displayed schematically in Fig. 2 and has been described earlier [21,22,34]. Helium atoms are emitted by a pulsed valve into an evacuated chamber, creating a pulsed supersonic beam. The ($1s$) ($2s$) 1S_0 metastable state of ${}^4\text{He}$ (He^* hereafter) is populated in an electric discharge near the orifice (diameter 0.2 mm) of the pulsed valve. The valve body is cooled to 10 K, resulting in a supersonic beam with a velocity of around 500 m/s [35]. To reduce the Doppler width of transitions to np Rydberg states, the central part of the supersonic beam is selected with

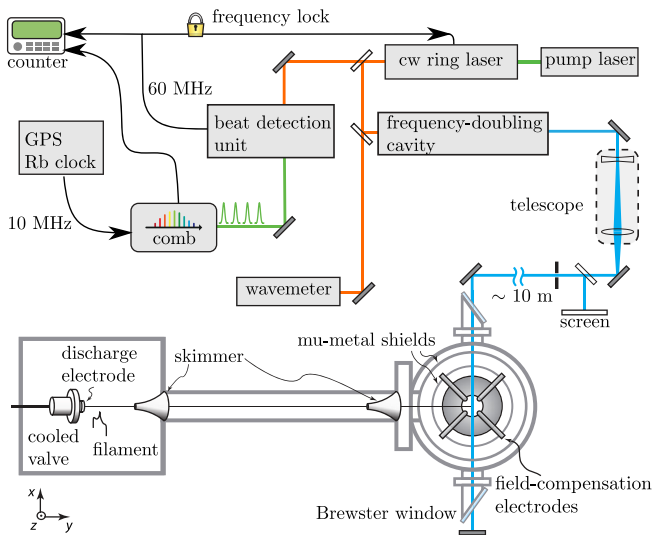


FIG. 2. Schematic diagram of the experimental setup. Top: laser system including the optical frequency comb used for frequency calibration and the external frequency-doubling cavity. Bottom left: valve and discharge electrodes used to generate the supersonic expansion of metastable helium. Bottom: vacuum chamber, where the He and laser beams cross within a double layer of magnetic shielding and electric-stray-field-compensation electrodes.

two skimmers having diameters of 3 mm and 0.8 mm and located 13 cm and 94 cm downstream from the nozzle orifice, respectively. In the interaction region, the atomic beam is crossed at near-right angles by two counterpropagating UV laser beams ($\lambda \approx 312$ nm). Photoexcitation is detected by pulsed-field ionization of the Rydberg states upon application of a pulsed potential difference of 4.5 kV across a 6-cm-long cylindrical stack of planar electrodes. The resulting electric field ionizes Rydberg states with $n \geq 24$ and extracts the He^+ ions toward a microchannel-plate detector. Spectra are recorded by monitoring the He^+ ion yield as a function of the laser frequency.

The UV laser radiation is generated by frequency doubling the output of a single-mode (linewidth about 1.5 MHz in the fundamental) continuous-wave tunable ring dye laser [21] in an external cavity using a β -barium-borate crystal. The ring dye laser is frequency offset locked to an optical frequency comb (Menlo, FC1500-250-WG) at a 60 MHz beat frequency f_{beat} [21]. The optical frequency comb is referenced to a GPS-disciplined Rb clock enabling a relative stability of 2×10^{-11} over the typical measurement time of 1 s needed to record a single data point [18]. This stability translates into a systematic uncertainty of 19 kHz in the UV. The laser frequency is scanned by changing the repetition rate of the frequency comb.

To cancel the first-order Doppler shift, the laser beam is retroreflected after crossing the supersonic beam containing He^* using a highly reflective mirror located 20 cm beyond the supersonic beam. A retroreflection angle of $180.000^\circ \pm 0.004^\circ$ is achieved by overlapping the beams at a distance of 10 m from the mirror using a spherical aperture of 1.4 mm diameter. A small deviation (typically around 0.2°) from 90° of the angle between the counterpropagating laser beams and the atomic beam ensures that each transition consists of two Doppler components (see Fig. 3), displaced from the central frequency by opposite shifts of around 10 MHz. The first-order Doppler-free transition frequency is determined as the mean of the frequencies of the two Doppler components. A telescope is used to loosely focus the forward-propagating laser beam onto the retroreflecting mirror over a focusing distance of 10 m, ensuring minimal wavefront-curvature broadenings [36]. The uncertainty of 0.004° in the retroreflection angle leads to a systematic uncertainty of $\sigma_{\text{D,sys}} = 80$ kHz. By recording several (N) spectra of each transition after realignment of the laser beams, this systematic uncertainty is converted into a statistical uncertainty with $\sigma_{\text{D,stat}} = \sigma_{\text{D,sys}}/\sqrt{N}$.

Stray magnetic fields in the photoexcitation volume are reduced to below 1 mG by using two concentric μ -metal shields. Stray electric fields are compensated using an electrode stack consisting of plane electrodes in the z direction and four additional pin electrodes for the lateral x and y directions. To this end the $102p^1P_1 \leftarrow 2s^1S_0$ transition is recorded for different fields applied along

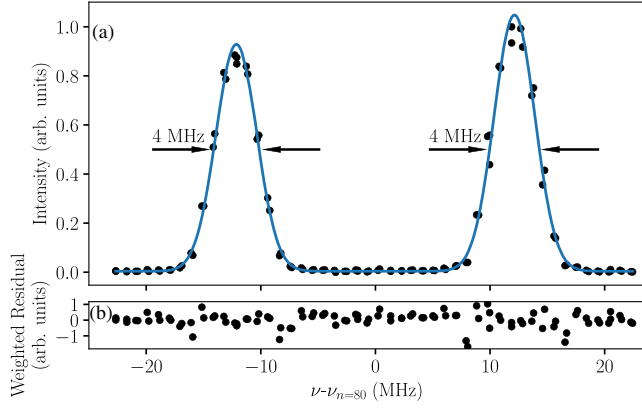


FIG. 3. (a) Spectrum of $80p \ ^1P_1 \leftarrow 2s \ ^1S_0$ transition (black dots) and a fit of two Gaussian profiles (blue line). (b) Weighted fit residuals (black dots). See text for details.

all three spatial directions, as explained in Ref. [37] and illustrated in Fig. 4. Because the Stark effect shifts the $np \leftarrow 2s \ ^1S_0$ transition frequencies to higher values, the minimum transition frequency corresponds to the optimal compensation. Fitting a parabolic curve to the obtained transition frequencies enables us to determine the zero-field position with an accuracy of 0.2 mV/cm.

Transitions to 21 different Rydberg states with principal quantum number n between 24 and 102 were measured. As an example, the spectrum of the $80p \ ^1P_1 \leftarrow 2s \ ^1S_0$ transition is shown in Fig. 3. The lineshape of both Doppler components is well described by a Gaussian profile with a full width at half maximum of 4 MHz. The parameters describing the overall double-peak lineshape comprise the two center positions, two maximum intensities, the

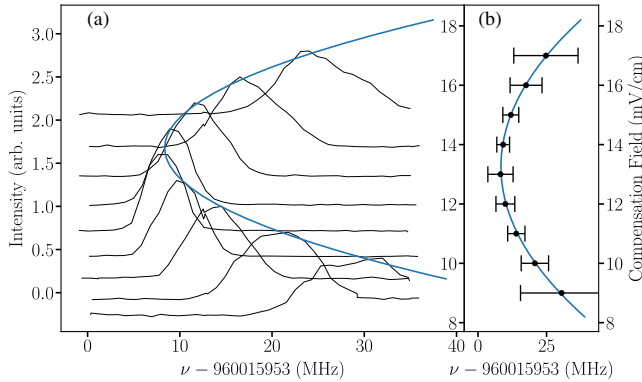


FIG. 4. Electric-stray-field compensation along the z direction. (a) Normalized spectra of one of the two Doppler components of the $102p \ ^1P_1 \leftarrow 2s \ ^1S_0$ transition of He, recorded at several values of the applied electric field. Each spectrum is shifted vertically to have its maximum value aligned to the value of the compensation field (secondary axis). (b) Transition frequencies of the individual measurements (black circles). The overlaying parabolic curves [blue lines in panels (a) and (b)] indicate the quadratic Stark shifts. The stray field is compensated at the apex of the parabolic curve (here, $F_z = 13.2(2)$ mV/cm).

linewidth, and a constant background offset. To account for the Poissonian nature of the ion-detection statistics when determining the line centers in a least-squares fit, the data points are weighted by the inverse signal intensity [38]. The weighted residuals are depicted in the lower panel of Fig. 3. Each line was recorded at least four times. For each recording, the laser frequency was scanned first up and then down to eliminate the effects of a residual hysteresis of the data acquisition system. The measurements were repeated several times on N different days, after full realignment of the laser beams. The frequency of a particular transition was obtained as the weighted average of all measurements, and its statistical uncertainty taken as the weighted standard deviation of the line centers divided by the square root of the number of independent measurements (\sqrt{N}). Typical results of a series of measurements of the $50p \leftarrow 2s$ transition are presented in the inset of Fig. 5.

The ionization energy of He^* is determined in a least-squares fit based on the Rydberg-Ritz formula [39]

$$E_n/(hc) = E_1(2 \ ^1S_0)/(hc) - \frac{R_{\text{He}}}{n^{*2}}. \quad (1)$$

In Eq. (1), $R_{\text{He}} = 109\,722.273\,486\,95(21) \text{ cm}^{-1}$ is the mass-dependent Rydberg constant, calculated according to Ref. [25] and $n^* = n - \delta(n)$. The n -dependent quantum defect is expressed as

$$\delta(n) = \delta_0 + \frac{\delta_2}{[n - \delta_0]^2} + \frac{\delta_4}{[n - \delta_0]^4} + \dots, \quad (2)$$

where the terms beyond δ_0 describe its energy dependence [30,40,41]. In the fits, we only included the parameters $E_1/(hc)$, δ_0 , δ_2 , and δ_4 because $\delta_{i \geq 6}$ remained undetermined.

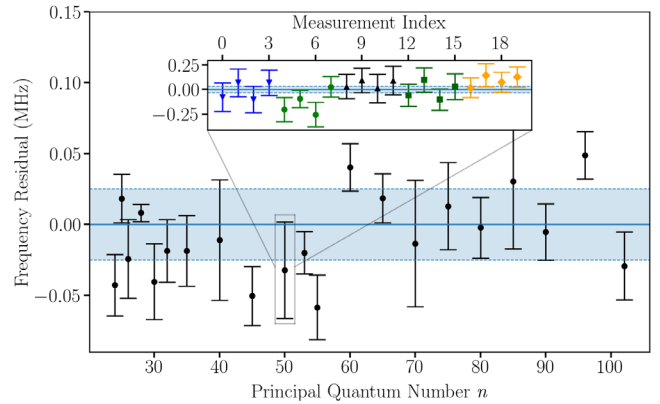


FIG. 5. Frequency residuals of the $np \ ^1P_1 \leftarrow 2s \ ^1S_0$ transitions relative to the values calculated using the Rydberg-Ritz formula. The blue-shaded area represents the statistical uncertainty of 25 kHz. The inset shows the frequency residuals of the $50p \ ^1P_1 \leftarrow 2s \ ^1S_0$ transition. Different colors and markers correspond to measurements of this transition carried out on different days, and the blue shaded area represents the standard deviation (35 kHz).

To account for the residual stray electric field after compensation, we followed the procedure introduced in Ref. [30] and included an additional term describing the quadratic Stark effect, which shifts the transition frequencies to the blue (see Fig. 4), according to

$$\Delta E_n = \frac{1}{2}\alpha|\mathbf{F}|^2, \quad (3)$$

where $\alpha = \alpha^*n^7$ is the n -dependent polarizability of the $S = 0$ np Rydberg states. The fit yielded residual stray electric fields of the order of 0.5 mV/cm, which we attribute to field inhomogeneities in the photoexcitation volume.

An overview of the uncertainties affecting individual transition frequencies is presented in Table I. The total statistical uncertainty of 25 kHz for the ionization energy results from the finite Doppler width, the number (N) of independent measurements, the quality of the alignment of the retroreflected beam, the quality of the lineshape model, the signal-to-noise ratio of the individual spectra, and the number of different transitions used for the extrapolation.

To estimate the systematic uncertainty (~ 20 kHz) for a single transition, the following effects were considered, as summarized in Table I.

Pressure shift.—The pressure shift results from collisional interactions of the slow Rydberg electron with neutral atoms [primarily He ($1s$) 2 1S_0 atoms] located inside the p Rydberg electron orbit [42]. For He, a pressure shift of 5.75 kHz/(10^{12} particles/cm 3) was measured by Amaldi and Segrè [43] and confirmed by Köhler *et al.* [44]. The He gas density at a distance of 106 cm from the nozzle is estimated to be $\leq 1.4 \times 10^{11}$ particles/cm 3 , which corresponds to a maximal pressure shift of ≤ 0.8 kHz.

First-order Doppler shift.—The residual first-order Doppler shift would represent a systematic uncertainty of 80 kHz for a single measurement. However, it is transformed into a statistical error, as explained above. The first-order Doppler shift represents the main contribution to the statistical uncertainties of the transition frequencies.

Second-order Doppler shift.—The second-order Doppler shift causes a redshift of the transition frequencies given by $-(\nu_0 v^2/2c^2) = -1.33(15)$ kHz and is compensated.

TABLE I. Overview of systematic shifts and uncertainties.

Source	Shift	Uncertainty
Pressure shift		<0.8 kHz
dc-Stark shift	Accounted for in model	
ac-Stark shift		<5 kHz
Second-order Doppler shift	-1.33 kHz	150 Hz
Photon-recoil shift	506 kHz	
Frequency calibration		19 kHz
σ_{sys}		<20 kHz

Photon-recoil shift.—The photon-recoil shift $h\nu_0^2/2mc^2$ is accurately known for each transition. To obtain the energy differences between the np 1P_1 and the $2s$ 1S_0 levels, this shift is subtracted from the observed transition frequencies.

Calibration error.—The accuracy of the frequency calibration is limited by the stability of the GPS-disciplined Rb clock of 2×10^{-11} over 1 s measurement time, which results in a systematic uncertainty of 19 kHz.

dc-Stark shift.—Typical residual stray electric fields are about 0.5 mV/cm in our experiment. Because we included the quadratic Stark shifts in our analysis, the Stark effect should not result in a systematic uncertainty. We verified this expectation by carrying out distinct extrapolation of the ionization energy using low- n ($n \leq 50$) Rydberg states, which are not significantly affected by the stray fields, and using high- n ($n \geq 50$) Rydberg states. The extrapolated values differed by 23 kHz, which is within the uncertainty limits of the determination.

ac-Stark shift.—ac-Stark shifts were assessed by measuring certain transitions at different laser powers. A reduction to 30% of the original laser power did not reveal any shift within the precision of our experiment.

Our final result for the ionization energy of the 2^1S_0 metastable state of helium is $E_1/h = 960\,332\,040.491(0.025)_{\text{stat}}(0.020)_{\text{sys}}$ MHz, with a total uncertainty of 32 kHz. The quantum-defect parameters of the np Rydberg states were determined to be $\delta_0 = -0.012\,1422(2)$, $\delta_2 = 0.007\,35(15)$, and $\delta_4 = 0.012\,4(29)$, and agree with earlier experimental [30] and theoretical [45] results.

Our new result for the ionization energy of the $2s$ 1S_0 metastable state of helium is compared with earlier results in Table II. It lies 2.6 MHz (1.5σ) above the theoretical values obtained by Drake and Yan [10] and by Pachucki *et al.* [11] which included the QED correction terms up to $\alpha^6 m$. The former experimental results lie above our value with deviations of -2.4σ [29] and -5.2σ [30] (-3.5σ including the correction mentioned in [31]).

TABLE II. Experimental (rows 1–4) and theoretical (rows 5–9) values of the ionization energy of the 2^1S_0 state.

	Ionization Energy/ h (MHz)
This work	960 332 040.491(32)
Sansonetti and Gillaspay [30]	960 332 041.612(210)
Bergeson <i>et al.</i> [31] ^a	960 332 041.282(222)
Lichten <i>et al.</i> [29]	960 332 040.862(150)
Drake [45]	960 332 039.9(25.0)
Morton <i>et al.</i> [46]	960 332 041.0(5.0)
Pachucki [47,48]	960 332 038.13(1.90)
Drake and Yan [10] ^b	960 332 037.9(1.7)
Pachucki <i>et al.</i> [11]	960 332 038.0(1.9)

^aReanalysis of measurements from Ref. [30].

^bIncludes QED corrections of order α^6 term calculated in Ref. [48].

TABLE III. Comparison of experimental and theoretical values [12,49] of the ionization energies of the 2^3S_1 , 2^3P (centroid), 3^3D_1 , and 3^1D_2 states in ^4He (in MHz) obtained by combining the 2^1S_0 ionization energy with the transition frequencies from Refs. [15–17,26,32,33].

	Experiment	This work + Ref	Theory	Reference	$\Delta E_{\text{I,exp-calc}}/h$
2^3S_1	1152 842 742.640(32)	[17]	1152 842 742.231(52)	[12]	0.409(61)
2^3P	876 106 247.025(39)	[15,17,32,33]	876 106 246.611(16)	[12]	0.414(42)
3^3D_1	366 018 892.638(65)	[17,26]	366 018 892.691(23)	[49]	−0.053(69)
3^1D_2	365 917 748.688(34)	[16]	365 917 748.661(19)	[49]	0.027(38)

In combination with transition frequencies measured for the $2^3S_1 \leftarrow 2^1S_0$ [17], $2^3P \leftarrow 2^3S_1$ [15,32,33], $3^3D_1 \leftarrow 2^3S_1$ [26] and $3^1D_2 \leftarrow 2^1S_0$ [16] intervals of He (see Fig. 1), our new result for the ionization energy of the 2^1S_0 state enables the determination of purely experimental values of the ionization energies of the 2^3S_1 , 2^3P , 3^3D_1 , and 3^1D_2 levels of He. The results are compared in Table III with the theoretical ionization energies of the 2^3S_1 and 2^3P states from [12] and of the 3^3D_1 and 3^1D_2 states from [49].

The discrepancies $(E_{\text{I,exp}} - E_{\text{I,calc}})/h$ in the ionization energies of the 2^3S_1 [409(61) kHz] and 2^3P [414(42) kHz] states are almost identical and significant at the 6.5σ and 10σ levels, respectively. In contrast, the ionization energies of the 3^3D_1 and 3^1D_2 levels are in agreement within the combined theoretical and experimental uncertainties.

Zalialiutdinov *et al.* [28] have recently pointed out that quantum-interference effects might reduce the frequency of the $3^3D_1 \leftarrow 2^3S_1$ transition reported in Ref. [26] by 510 kHz, which would result in an 8σ discrepancy $\Delta\nu_{\text{I,exp-calc}}$ of $-563(69)$ kHz for the 3^3D_1 state. We note that a second experimental value of the $3^3D_1 \leftarrow 2^3S_1$ interval can be derived by adding the weighted average of the $2^3P_0 \leftarrow 2^3S_1$ interval from Zheng *et al.* [15] and Cancio Pastor *et al.* [32] [276 764 094 673(23) kHz] to the $3^3D_1 \leftarrow 2^3P_0$ interval from Luo *et al.* [14] [510 059 755 352(28) kHz]. The result [786 823 850 025(36) kHz] agrees with the “uncorrected” value of Dorrer *et al.* [26] [786 823 850 002(56) kHz].

This analysis supports the suggestion by Patkóš *et al.* [12] of a so far unrecognized QED shift of about 500 kHz affecting the theoretical ionization energies of the 2^3S_1 and 2^3P states. Our new results quantify this shift to be 409(61) kHz and indicate the necessity to calculate the ionization energy of the 2^1S_0 state of ^4He for direct comparison. Given the importance of the spectroscopy of He in the determination of particle properties and fundamental constants [11,12,24], efforts towards understanding the reasons for the large discrepancies between experimental and theoretical ionization energies of states of the $n = 2$ and 3 manifolds of He should be given a high priority.

We thank Nicolas Hölsch for advice and discussions concerning the data analysis. This work is supported by the

Swiss National Science Foundation through the Sinergia-program (Grant No. CRSII5-183579) and the Grant No. 200020B-200478.

*frederic.merkt@phys.chem.ethz.ch

- [1] A. Antognini *et al.*, *Science* **339**, 417 (2013).
- [2] A. Beyer, L. Maisenbacher, A. Matveev, R. Pohl, K. Khabarova, A. Grinin, T. Lamour, D. C. Yost, T. W. Hänsch, N. Kolachevsky, and T. Udem, *Science* **358**, 79 (2017).
- [3] H. Fleurbaey, S. Galtier, S. Thomas, M. Bonnaud, L. Julien, F. Biraben, F. Nez, M. Abgrall, and J. Guéna, *Phys. Rev. Lett.* **120**, 183001 (2018).
- [4] N. Bezginov, T. Valdez, M. Horbatsch, A. Marsman, A. C. Vutha, and E. A. Hessels, *Science* **365**, 1007 (2019).
- [5] W. Ubachs, *Science* **370**, 1033 (2020).
- [6] A. Grinin, A. Matveev, D. C. Yost, L. Maisenbacher, V. Wirthl, R. Pohl, T. W. Hänsch, and T. Udem, *Science* **370**, 1061 (2020).
- [7] V. I. Korobov, L. Hilico, and J.-P. Karr, *Phys. Rev. Lett.* **118**, 233001 (2017).
- [8] S. Alighanbari, G. S. Giri, F. L. Constantin, V. I. Korobov, and S. Schiller, *Nature (London)* **581**, 152 (2020).
- [9] S. Patra, M. Germann, J.-P. Karr, M. Haidar, L. Hilico, V. I. Korobov, F. M. J. Cozijn, K. S. E. Eikema, W. Ubachs, and J. C. J. Koelemeij, *Science* **369**, 1238 (2020).
- [10] G. W. Drake and Z. C. Yan, *Can. J. Phys.* **86**, 45 (2008).
- [11] K. Pachucki, V. Patkóš, and V. A. Yerokhin, *Phys. Rev. A* **95**, 062510 (2017).
- [12] V. Patkóš, V. A. Yerokhin, and K. Pachucki, *Phys. Rev. A* **103**, 042809 (2021).
- [13] R. van Rooij, J. S. Borbely, J. Simonet, M. D. Hoogerland, K. S. E. Eikema, R. A. Rozendaal, and W. Vassen, *Science* **333**, 196 (2011).
- [14] P.-L. Luo, J.-L. Peng, J. Hu, Y. Feng, L.-B. Wang, and J.-T. Shy, *Phys. Rev. A* **94**, 062507 (2016).
- [15] X. Zheng, Y. R. Sun, J.-J. Chen, W. Jiang, K. Pachucki, and S.-M. Hu, *Phys. Rev. Lett.* **119**, 263002 (2017).
- [16] Y.-J. Huang, Y.-C. Guan, Y.-C. Huang, T.-H. Suen, J.-L. Peng, L.-B. Wang, and J.-T. Shy, *Phys. Rev. A* **97**, 032516 (2018).
- [17] R. J. Rengelink, Y. van der Werf, R. P. M. J. W. Notermans, R. Jannin, K. S. E. Eikema, M. D. Hoogerland, and W. Vassen, *Nat. Phys.* **14**, 1132 (2018).
- [18] N. Hölsch, M. Beyer, E. J. Salumbides, K. S. E. Eikema, W. Ubachs, C. Jungen, and F. Merkt, *Phys. Rev. Lett.* **122**, 103002 (2019).

- [19] M. Puchalski, J. Komasa, P. Czachorowski, and K. Pachucki, *Phys. Rev. Lett.* **122**, 103003 (2019).
- [20] D. Ferenc, V. I. Korobov, and E. Mátyus, *Phys. Rev. Lett.* **125**, 213001 (2020).
- [21] L. Semeria, P. Jansen, G.-M. Camenisch, F. Mellini, H. Schmutz, and F. Merkt, *Phys. Rev. Lett.* **124**, 213001 (2020).
- [22] P. Jansen, L. Semeria, and F. Merkt, *J. Chem. Phys.* **149**, 154302 (2018).
- [23] J.-P. Karr, D. Marchand, and E. Voutier, *Nat. Rev. Phys.* **2**, 601 (2020).
- [24] G. W. F. Drake, *J. Phys. B* **53**, 223001 (2020).
- [25] E. Tiesinga, P. J. Mohr, D. B. Newell, and B. N. Taylor, Fundamental Physical Constants from NIST (2018), <http://physics.nist.gov/constants>.
- [26] C. Dorrer, F. Nez, B. de Beauvoir, L. Julien, and F. Biraben, *Phys. Rev. Lett.* **78**, 3658 (1997).
- [27] J. J. Krauth *et al.*, *Nature (London)* **589**, 527 (2021).
- [28] T. Zalialiutdinov, A. Anikin, and D. Solov'yev, *arXiv*: 2103.14365v1.
- [29] W. Lichten, D. Shiner, and Z.-X. Zhou, *Phys. Rev. A* **43**, 1663 (1991).
- [30] C. J. Sansonetti and J. D. Gillaspay, *Phys. Rev. A* **45**, R1 (1992).
- [31] S. D. Bergeson, A. Balakrishnan, K. G. H. Baldwin, T. B. Lucatorto, J. P. Marangos, T. J. McIlrath, T. R. O'Brien, S. L. Rolston, C. J. Sansonetti, J. Wen, N. Westbrook, C. H. Cheng, and E. E. Eyler, *Phys. Rev. Lett.* **80**, 3475 (1998).
- [32] P. Cancio Pastor, G. Giusfredi, P. De Natale, G. Hagel, C. de Mauro, and M. Inguscio, *Phys. Rev. Lett.* **92**, 023001 (2004); **97**, 139903(E) (2006).
- [33] P. Cancio Pastor, L. Consolino, G. Giusfredi, P. De Natale, M. Inguscio, V. A. Yerokhin, and K. Pachucki, *Phys. Rev. Lett.* **108**, 143001 (2012).
- [34] P. Jansen, L. Semeria, and F. Merkt, *Phys. Rev. Lett.* **120**, 043001 (2018).
- [35] M. Motsch, P. Jansen, J. A. Agner, H. Schmutz, and F. Merkt, *Phys. Rev. A* **89**, 043420 (2014).
- [36] A. Beyer, L. Maisenbacher, A. Matveev, R. Pohl, K. Khabarova, Y. Chang, A. Grinin, T. Lamour, T. Shi, D. C. Yost, T. Udem, T. W. Hänsch, and N. Kolachevsky, *Opt. Express* **24**, 17470 (2016).
- [37] A. Osterwalder and F. Merkt, *Phys. Rev. Lett.* **82**, 1831 (1999).
- [38] M. Beyer, N. Hölsch, J. A. Agner, J. Deiglmayr, H. Schmutz, and F. Merkt, *Phys. Rev. A* **97**, 012501 (2018).
- [39] W. Ritz, *Phys. Z.* **4**, 406 (1903).
- [40] G. W. F. Drake and R. A. Swainson, *Phys. Rev. A* **44**, 5448 (1991).
- [41] M. Peper, F. Helmrich, J. Butscher, J. A. Agner, H. Schmutz, F. Merkt, and J. Deiglmayr, *Phys. Rev. A* **100**, 012501 (2019).
- [42] E. Fermi, *Il Nuovo Cimento (1924–1942)* **11**, 157 (1934).
- [43] E. Amaldi and E. Segrè, *Il Nuovo Cimento* **11**, 145 (1934).
- [44] A. M. Köhler, R. Reininger, V. Saile, and G. L. Findley, *Phys. Rev. A* **35**, 79 (1987).
- [45] G. W. F. Drake, *Phys. Scr.* **T83**, 83 (1999).
- [46] D. C. Morton, Q. Wu, and G. W. Drake, *Can. J. Phys.* **84**, 83 (2006).
- [47] K. Pachucki, *Phys. Rev. A* **74**, 022512 (2006).
- [48] K. Pachucki, *Phys. Rev. A* **74**, 062510 (2006).
- [49] V. A. Yerokhin, V. Patkóš, M. Puchalski, and K. Pachucki, *Phys. Rev. A* **102**, 012807 (2020).